

Instability of shock-induced nozzle flow separation

Andrew D. Johnson and Dimitri Papamoschou

*Department of Mechanical and Aerospace Engineering, University of California-Irvine,
4200 Engineering Gateway, Irvine, California 92697-3975, USA*

(Received 18 August 2009; accepted 3 November 2009; published online 8 January 2010)

We investigate experimentally the causes of jet plume instability and enhanced mixing observed in the exhaust of shock-containing convergent-divergent nozzles. Key features of the internal flow are the separation shock, separation shear layers, and pattern of alternating expansion and compression waves downstream of the shock. We focus on two possible reasons for this instability—the motion of the separation shock and the wave pattern downstream of the shock. The nozzle flow was generated in a planar facility with variable area ratio and pressure ratio, and the motion of the shock was tracked using time-resolved wall pressure measurements. The isolated effect of the wave pattern was investigated in a separate facility wherein a sonic shear layer, simulating the nozzle separation shear layer, was disturbed with compression and expansion waves emanating from a wavy wall. In both instances, the instability of the shear layer was characterized by time-resolved measurements of the total pressure. In the nozzle flow, the amplitude of shock motion increases with shock strength. Correlation of shock motion with shear layer total pressure is virtually absent for weak shocks but becomes significant for strong shocks. However, impingement of stationary waves on the shear layer had no impact on its growth rate. We conclude that the enhanced shear layer instability is strongly coupled to shock motion, and that the wave pattern by itself is not a cause of enhanced mixing. The occurrence of asymmetric separation at large shock strengths is a further contributor to the enhancement of instability. © 2010 American Institute of Physics. [doi:10.1063/1.3278523]

I. INTRODUCTION

The modern study of shock-containing nozzle flows is typically motivated by the desire to suppress the negative characteristics associated with them. The occurrence of the side loads during the startup of rocket nozzles is just one example where the aerodynamic forces caused by a shock can result in severe structural damages.¹ The present study approaches the same problem from an alternative perspective, investigating overexpanded nozzle flow for its potential application in high speed mixing enhancement. The motivation is exemplified by the flow visualizations of Figs. 1 and 2. In Fig. 1, an annular jet exhausting at a fully expanded Mach number 0.9 is destabilized by changing the shape of the nozzle from convergent to convergent-divergent. In Fig. 2, a similar annular stream is used to destabilize a round jet surrounded by the unstable annular stream. In both instances, the flow conditions [nozzle pressure ratio (NPR) and area ratio] are such that a separation shock is formed inside the annular nozzle.² A series of small-scale experiments in our laboratory and at other institutions has quantified this type of mixing enhancement in a variety of nozzles using mean velocity surveys, hot-wire anemometry, and flow visualization.^{2–5} Benefits relative to mechanical mixers include the simplicity of the flow path and the fact that arrangements like the nozzle of Fig. 2 are already present in the exhaust of turbofan engines; thus, a minor reshaping of the fan nozzle—possibly via active control—could lead to mixing enhancement for reduction of thermal plume signature, for example.

The small-scale tests could not answer the physical reasons for the observed mixing enhancement—apart from the

knowledge that the nozzle operating conditions necessitated the formation of a shock wave inside the nozzle. It became evident that an investigation of the basic phenomenon of supersonic nozzle flow separation was necessary to obtain insight into the fundamental causes of the plume instability. Below we summarize key findings of our past studies as well as relevant works by other investigators. Figure 3 presents an instantaneous schlieren visualization of shock-induced separation in a planar nozzle having an area ratio of 1.5 and operating at NPR of 1.5. The salient features of the flow are presented in the simplified diagram of Fig. 4.⁶ Near the wall, the separation shock consists of incident and reflected oblique waves that merge into a Mach stem at the triple point. This is the so-called lambda foot of the shock. The adverse pressure gradient through the shock forces the incoming boundary layer to separate, forming separation regions downstream. The oblique shock structures are of the “weak” type resulting in low supersonic flow downstream while the flow immediately past the Mach stem is subsonic. The trailing shocks reflect from the separation shear layers as expansion fans that propagate across the test section to the opposite shear layers where they are reflected again as compression waves. Slipstreams emerging from the triple points form a convergent-divergent channel which, in concert with the expansion fans, accelerates the subsonic flow downstream of the normal portion of the shock to supersonic speed, as illustrated in the schematic of Fig. 4. The wave reflections continue downstream, resulting in a series of alternating regions of expansion and compression through the separation jet. Numerical investigations by Wilmoth and Levitt⁷ and by Hamed and Voyatzis^{8,9} showed an agreement

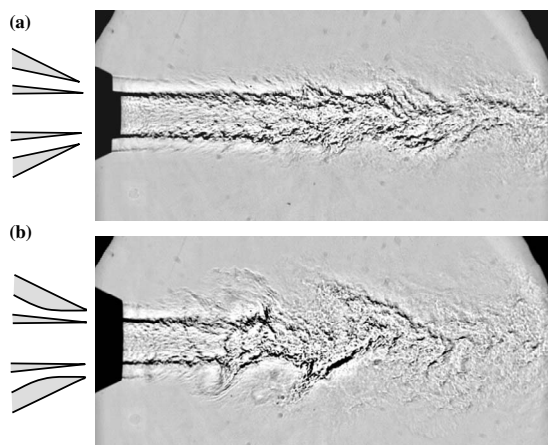


FIG. 1. Air exhausting from an annular nozzle at NPR=1.7. (a) Convergent nozzle; (b) convergent-divergent nozzle.

on this basic structure of the shock separation. Analytical models of overexpanded nozzle flowfields by Li and Ben-Dor¹⁰ and by Romine¹¹ have been formulated based on principal flow features just described, although these models generally apply to rapidly expanding nozzles, such as in the case of rocket nozzles, or in cases where the shock is located at the nozzle exit. The limiting assumption of these models is that the pressure just downstream of the separation point is equal to the ambient pressure. Experimentally, this assumption has been shown to be invalid in the case of gradually expanding convergent-divergent nozzles such as those studied here.⁶

At high NPRs (reservoir pressure divided by the ambient pressure, $NPR = p_{res}/p_a$) and exit-to-throat area ratios A_e/A_t , the separation occurs asymmetrically with one lambda foot being larger than the other.⁶ When separation occurs asymmetrically, the orientation of the asymmetry is steady during a given experiment; however it can change from one experiment to the next suggesting that it is sensitive to the startup conditions. Papamoschou *et al.*⁶ attributed this behavior to the “Coanda effect” whereby a jet surrounded by or adjacent

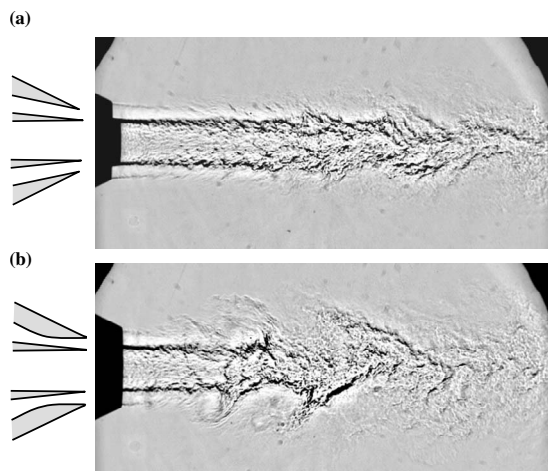


FIG. 2. Primary jet flow at Mach 0.9 surrounded by an annular secondary flow at NPR=1.7. (a) Secondary nozzle is convergent; (b) secondary nozzle is convergent-divergent.

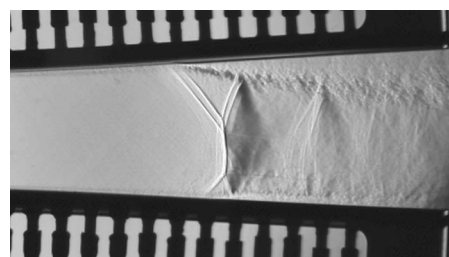


FIG. 3. Schlieren photograph of the internal nozzle flowfield undergoing asymmetric separation.

to a solid surface attaches to that surface. A computational investigation by Xiao *et al.*¹² successfully predicted this asymmetry numerically by solving the Reynolds averaged Navier–Stokes equations with a two equation $k-\omega$ turbulence model. This study also showed a rapid expansion downstream of the Mach stem followed by compression, further supporting the flow structure outlined in Fig. 4. The wave pattern of Fig. 4 is similar to that shock-cell pattern formed in the “traditional” case of a highly overexpanded nozzle wherein the entire nozzle flow is supersonic, oblique shocks originate from the nozzle lip, and the shocks undergo Mach reflection from a Mach stem. The principal difference is that, in the case of internal shock formation, the separation oblique shock is not anchored at a specific point. This allows the shock to oscillate, whereas in the traditional overexpansion the shock origin is substantially fixed at the nozzle lip. Other differences include the asymmetry and decay rate of the shock cell strength.

Flow visualization combined with time-resolved wall pressure measurements obtained at the feet of the shock wave indicates that the shock oscillates in a pistonlike manner at low frequency.¹³ Wall pressure spectra suggest that the motion is broadband with no preferred frequencies being excited. The source of unsteadiness in shock-induced separated flowfields is a subject that has been studied extensively and yet remains controversial. The debate is centered around the low-frequency nature of the shock oscillation, the oscillation frequency being often lower than the characteristic frequencies of turbulence in the vicinity of the shock. A comprehensive literature review by Dussauge *et al.*¹⁴ and Dussauge and Piponnier¹⁵ suggests that depending on the particular experiment, one can argue that upstream or downstream conditions

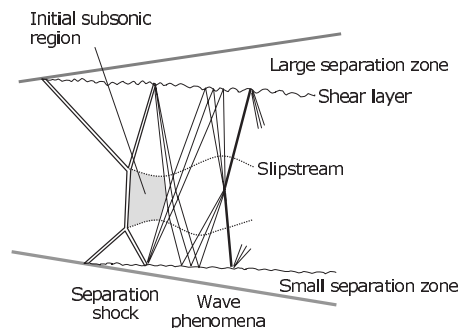


FIG. 4. Schematic of principal phenomena in supersonic nozzle flow separation (based on Ref. 4).

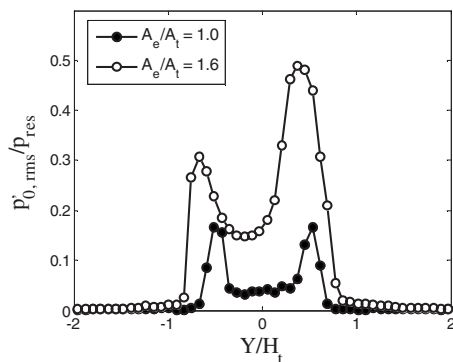


FIG. 5. Transverse profile of rms fluctuation of total pressure in the jet plume at $X/H_t=0.5$ for a straight nozzle ($A_e/A_t=1$) and a convergent-divergent nozzle ($A_e/A_t=1.6$) at $\text{NPR}=1.8$.

explain the low frequency motion. This implies that the shock wave motion may be rather sensitive to the geometric conditions of separation.

Bourgoing and Reijasse¹⁶ examined unsteady shock behavior in a Mach 2 planar nozzle facility. The mean shock location was controlled by adjusting the height of a second throat positioned downstream of the test section. Similar to our past experiments, both symmetric and asymmetric separations were observed. It was found that the asymmetry could be induced by increasing the roughness on one of the walls near the throat region of the nozzle, thereby changing the conditions in the upstream boundary layer. For cases where asymmetry was induced by roughness, the intensity of wall pressure fluctuations measured downstream of the shock increased significantly. Wall pressure spectra measured near the recirculation regions showed two spectral bumps, unlike the relatively broadband wall pressure spectra obtained in our past experiments.^{6,13} This difference is likely attributed to the reattachment of the separation shear layers in the presence of a second throat, giving rise to the possibility of aeroacoustic resonance behavior.

In a related study of transonic resonance in shock-containing convergent-divergent nozzles, Zaman *et al.*¹⁷ found evidence of harmonic shock motion that resulted in strong acoustic tones similar to those found in screeching nozzles. The resonant behavior showed similarity to the acoustic resonance of a conical section having one end closed and the other end open. One interesting facet of this phenomenon is that the acoustic tones could be suppressed by tripping the boundary layer upstream of the shock. This suggests that the harmonic shock motion is associated with a laminar boundary layer upstream of the shock separation. In the current experiments, where the boundary layer was fully turbulent, we did not observe aeroacoustic resonance and there was no dominant wavelength of the shock oscillation. It is noteworthy that mixing enhancement occurs with or without resonant tones.⁵

In cases with asymmetric separation, the large separation shear layer develops rapidly, with eddies occupying as much as 50% of the test section height near the nozzle exit. At the nozzle exit, the turbulence fluctuations are much higher than for a jet issuing from a straight (or convergent) nozzle. This is illustrated by Fig. 5 which plots the transverse distribution

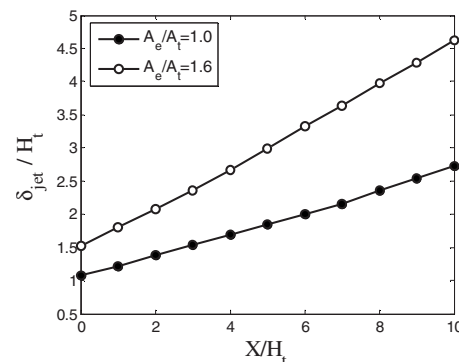


FIG. 6. Jet thickness distribution for a straight nozzle ($A_e/A_t=1$) and convergent-divergent nozzle ($A_e/A_t=1.6$) at $\text{NPR}=1.8$.

of rms fluctuation of total pressure for area ratio of 1.0 (no divergence) and area ratio of 1.6. The fluctuation intensity increases threefold as the nozzle shape changes from straight to convergent-divergent. Note the asymmetric distribution of the rms total pressure, reflecting the asymmetry of the flow inside the nozzle. It is this amplification of instability that is responsible for the enhanced mixing exemplified by Figs. 1 and 2. Mean flow surveys of the plume have shown that increases in the rms fluctuation of total pressure at the nozzle exit are correlated with significant increases in jet growth rate, evident by the increased slope of the jet thickness distribution curves in Fig. 6 for the same cases compared in Fig. 5. Numerical predictions using a shear stress transport turbulence model showed close agreement with these experimental results with increased levels of turbulent kinetic energy near the nozzle exit and improved mixing in the plume for cases where asymmetric separation occurred.¹⁸

Experiments using time-resolved pressure measurements showed that the total pressure fluctuation in the large separation shear layer correlates well with wall pressure fluctuations measured at the mean shock location, indicating a possible connection between shock unsteadiness and shear layer instability.⁹ However, the conditions of those experiments were limited and reliance on a single probe to determine shock motion is unsatisfactory. Further, an additional source of instability may be the alternating pattern of expansion and compression waves downstream of the main shock (Fig. 4). While numerous studies have focused on the receptivity of a shear layer to a field of alternating compressions and expansions, these studies have generally considered cases of higher Mach numbers than are relevant here.^{19,20} It should be noted that the small separation shear layer is subject to the same physics as the large separation shear layer. This suggests that the asymmetric configuration provides the space for instability waves in the larger separation shear layer to grow while growth in the small separation shear layer remains suppressed due to the close proximity of the nozzle wall.

The experiments conducted in the current investigation were designed to identify the primary mechanisms that contribute to the instability in the large separation shear layer. Specifically, the role of the unsteady shock motion as well as the succession of alternating expansion and compression waves downstream of the shock has been scrutinized. A sig-

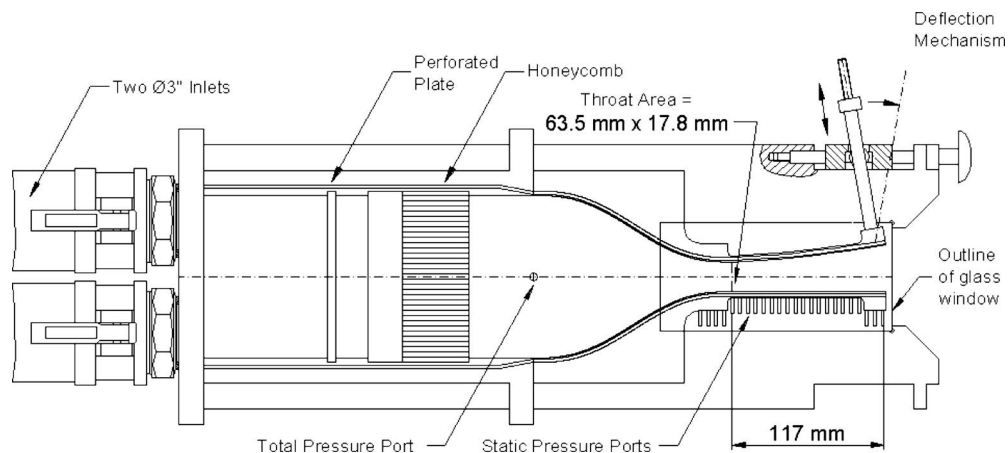


FIG. 7. Schematic of apparatus for the study of supersonic nozzle flow separation and shock unsteadiness.

nificant part of the investigation involved measuring the shock motion using an array of pressure transducers. The overall objective was to obtain an improved understanding of the underlying physics in supersonic nozzle flow separation so that it can be utilized more effectively for practical applications in high speed mixing.

II. EXPERIMENT

A. Test facilities

The primary facility utilized in this investigation, shown in Fig. 7, was designed to allow versatility in the study of nozzle flow. It incorporates two flexible plates forming the upper and lower walls of the nozzle that can be shaped using two sets of actuators located at the end of each plate. Adjusting the transverse force and moment applied to each wall allows variation in the exit-to-throat area ratio (A_e/A_t), nozzle contour, and maximum wall angle. The sidewalls of the nozzle test section consist of large optical windows to provide visualization of the entire internal flowfield. The nominal test section dimensions are 17.8 mm in height, 63.5 mm in width, and 117 mm in length from throat to exit. The apparatus is supplied by a pressure-regulated air supply capable of obtaining NPRs ($\text{NPR} = p_{\text{res}}/p_a$) up to 3.5 allowing for comprehensive study of various nozzle flows from subsonic, to shock-containing, to shock-free flow.

An existing compressible shear layer facility provided the means of simulating the conditions of the separation shear layer and evaluating the isolated effect of the shear layer being subjected to an alternating stationary wave pattern. The test section dimensions of this facility are 38 mm in height, 63 mm in width, and 300 mm in length, with optical glass sidewalls for visual access. The air is supplied by the same pressure regulated system as the nozzle facility. Static ports along the lower wall of the facility were monitored using a Scanivalve Model SSS-48 mechanical pressure multiplexer to ensure that the shear layer was not subject to favorable or adverse pressure gradients. The axial pressure distribution was controlled by adjusting the divergence angle of the upper and lower walls of the facility. The alternating series of expansion and compression waves was generated by making the upper wall of the test section sinusoidal with a

wavelength of 20 mm and a crest to trough amplitude of 1.5 mm. These dimensions were chosen in order to obtain a wave pattern that represented those seen in schlieren images of the separated nozzle flow.

B. Flow visualization

A spark schlieren system was employed in order to visualize the flowfields. This system was aligned on a mobile support table that could be coupled with either the nozzle facility or the shear layer facility. The light source was a 20 ns spark generated by a Xenon Model N787 nanopulser. The optics setup utilized 150 mm lenses with a focal length of 1 m to collimate the beam of light through the test section. A portion of the light was intercepted by an adjustable pinhole placed at the focal point of the emerging beam of light. Images were obtained using a charged coupled device camera (Sony, Cybershot) with a spatial resolution of 2560×1712 pixels.

C. Time-resolved diagnostics

This investigation utilized time-resolved measurements of the nozzle wall pressure and of the total pressure in the flow downstream of the shock. All the measurements used piezoelectric pressure transducers (Endevco Model 8507C-15) with 2 mm diameter sensors and frequency response of 30 kHz. Figure 8 depicts the layout of the transducers.

Four transducers were mounted flush along the upper

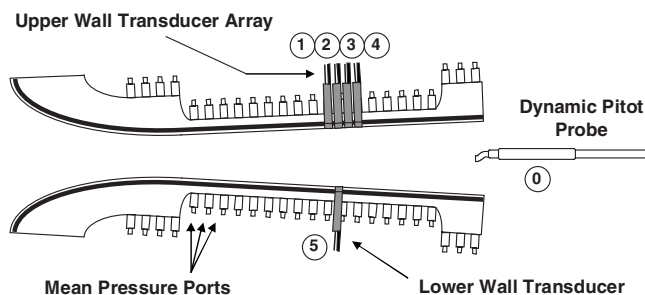


FIG. 8. Diagnostic setup of nozzle.

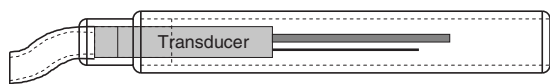


FIG. 9. Design of dynamic Pitot probe showing protective S-shaped inlet.

wall of the nozzle and were equally spaced to span a total distance of 12.7 mm from the center of the first probe to the center of the final probe. This distance corresponded to the estimated range of shock motion for the configurations of interest based on schlieren photography. The resulting array provides the instantaneous wall pressure distribution caused by the shock foot which is then used to track the longitudinal position of the shock foot along the nozzle wall. The details of this tracking procedure are provided in Sec. III. A fifth probe was mounted on the lower wall opposite the second probe of the upper-wall array. In addition to providing valuable quantitative information about the fluctuating flowfield, the fifth wall probe measurement was used in conjunction with the wall array measurement to verify the orientation of the shock asymmetry for a given run by exploiting the fact that the larger lambda foot extends further upstream than the smaller lambda foot.

A dynamic Pitot probe was used to measure the impact pressure, and its fluctuations, downstream of the shock. Given that this flow field is mildly supersonic at most, the impact pressure is practically identical to the total pressure p_0 . In the absence of time-resolved velocity measurements (which are very difficult for this high-speed flowfield), we use the fluctuations in total pressure to characterize the unsteadiness of the flow. The dynamic Pitot probe, depicted in Fig. 9, consists of a piezoelectric transducer oriented against the flow with an S-shaped protective inlet that prevents collision of particulates in the air with the transducer face. The length of the inlet is 8 mm and its inner diameter is 1.7 mm. The inlet introduces distortions in the frequency response of the probe that needs to be accounted for when calculating statistics such as the autospectra and variance of p'_0 . The distortion was determined by extensive testing of the transducer, with and without the protective inlet, placed transversely in stagnation-point flows with various amplitudes of pressure fluctuations. For all amplitudes, the fundamental tone of the distortion spectrum peaked at 10.7 kHz. Correction procedures, detailed in Ref. 11, were implemented for removing the distortion from the autospectrum of the pressure fluctuations and from the resulting computation of the variance.

All six transducers were sampled simultaneously at a sampling rate of 200 kS/s per channel for the duration of 1 s. A fourth-order low pass filter with 80 kHz corner frequency was installed in the amplifier to prevent effects of aliasing. Spectra were computed using a 4096-point fast Fourier transform resulting in a frequency resolution of 48.8 Hz. Cross correlations are normalized by the respective variances and cross-spectra are presented in the normalized form of coherence. Frequency f and time lag τ are normalized in the nozzle experiments using the throat height H_t , and the per-

TABLE I. Test configurations for the nozzle experiments.

Case	Nozzle area ratio A_e/A_t	Nozzle pressure ratio $\text{NPR}=p_{\text{res}}/p_a$	Shock strength $\Delta p/p$
1	1.4	1.45	1.38
2	1.5	1.55	1.76
3	1.6	1.70	2.08
4	1.7	1.90	2.30

fectly expanded exit velocity U_p , and in the shear layer experiments using the height of the upper stream H_u , and the velocity of the upper stream U_u .

D. Flow conditions

The nozzle experiments involved four combinations of nozzle area ratio and pressure ratio that resulted in a progressively stronger shock situated at the midpoint of the upper-wall transducer array (Fig. 8). This corresponds to a mean shock position of approximately three throat heights upstream of the nozzle exit ($X/H_t=-3.0$, see Fig. 18 for the coordinate system). The combinations of NPR and A_e/A_t , and resulting shock strength, are listed in Table I. The shock strength is given by the normal shock relation

$$\frac{\Delta p}{p} = \frac{2\gamma}{\gamma+1}(M_s^2 - 1), \quad (1)$$

with the shock Mach number M_s based on the area ratio at the mean location of the Mach stem, A_s/A_t . The Reynolds number based on throat height and perfectly expanded exit conditions ranged from 3.53×10^5 (case 1) to 5.23×10^5 (case 4). In cases where asymmetry is significant, the upper wall is associated with the large separation region and the lower wall with the small separation region. The Reynolds number based on nozzle length from throat to separation point ranged from 1.45×10^6 to 1.78×10^6 , corresponding to a fully turbulent boundary layer. The turbulent state of the boundary layer was evident from nanosecond schlieren photography such as the image of Fig. 3.

The shear layer experiments were designed to simulate the conditions of the separation shear layer. The separation shear layer is formed between a high-speed stream that is approximately sonic and a low speed that is practically at zero velocity (recirculation region). These conditions have been replicated in the compressible shear layer facility by having the upper stream entering the test section at Mach 1 and the lower stream quiescent. The upper stream was supplied by a convergent nozzle operating at the sonic pressure ratio of 1.893, with the pressure in the lower stream being approximately equal to the ambient pressure, $p_l \approx p_a$. The Reynolds number based on the height and the velocity of the upper stream was 5.19×10^5 . The objective of the experiment was to assess the impact of the alternating wave pattern on the shear layer instability, and therefore comparisons were made between a baseline case having a flat upper wall and test case having a wavy upper wall, as detailed in Sec. II A. The “mean” channel height was the same for both cases, and the operating conditions were identical as well.

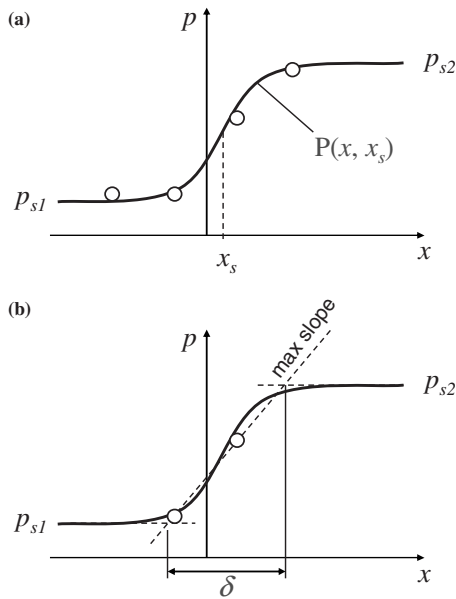


FIG. 10. Illustration of shock fitting routine. (a) Least-squares fit of function $P(x, x_s)$ through the data; (b) definition of shock thickness.

III. TRACKING OF THE SHOCK POSITION

Time-resolved measurement of the shock motion was an essential aspect of this investigation. Even though an array of transducers was used (Fig. 8), the limited spatial resolution of the measurement (dictated by probe sensor size) necessitated fitting an appropriate function through the instantaneous array data. To ensure the robustness of shock tracking procedure, we compare two methods for time-resolved tracking of the shock motion, each method using a different function for capturing the pressure rise across the shock.

A. Method I

The wall pressure “footprint” of the separation shock has a finite region because of its lambda foot structure. Consequently, the wall pressure distribution across the shock is smooth. Considering the narrow vicinity around the shock, we can approximate this pressure distribution using a hyperbolic tangent function of the form

$$P(x, x_s) = \frac{p_{s2} + p_{s1}}{2} + \frac{p_{s2} - p_{s1}}{2} \tanh \left[\frac{2}{\delta} (x - x_s) \right]. \quad (2)$$

It should be noted that x refers to the coordinate along the nozzle wall and not the axial direction X . The parameters of this distribution are the pressures p_{s1} and p_{s2} before and after the jump, respectively, the thickness of the distribution δ , and the shock position x_s . The distribution is illustrated in Fig. 10(a), and the definition of thickness in Fig. 10(b). The factor of 2 in the argument of the tanh is consistent with the definition of thickness given below.

The pressure transducers provide $p(x_i) = p_i$ for a given time at their four discrete locations, $x_1 \cdots x_4$. We use the experimental measurements of p_i to fit the distribution of Eq. (2) using a nonlinear least-squares scheme. The amplitudes p_{s1} and p_{s2} typically correspond to the instantaneous measurements of the minimum and maximum values of the array.

In the rare occurrences of the shock position x_s nearing the boundaries of the wall array, the mean (time-averaged) pressure of the first or last probes was used in place of the instantaneous measurements in order to extrapolate the model curve beyond the physical range of the array. The thickness δ is based on the maximum gradient between any two consecutive points in the measured distribution as follows:

$$\delta = (p_{s2} - p_{s1}) \left/ \left(\frac{p_{i+1} - p_i}{x_{i+1} - x_i} \right) \right|_{\max}. \quad (3)$$

The minimization process requires that we first guess the position of the shock x_s , and then correct this value iteratively until the error between the theoretical and actual pressure distributions is minimized. To obtain the appropriate correction we define the error vector

$$e_i = p_i - P(x_i, x_s). \quad (4)$$

Next we obtain a linearized estimate for the correction dx_s that minimizes the error vector by computing

$$dx_s = J_i^{-1} e_i, \quad (5)$$

where J is the Jacobian matrix

$$J_i = \frac{\partial}{\partial x_s} P(x_i, x_s). \quad (6)$$

This correction is then applied to the original guess, via Eq. (7), in order to obtain a new guess for the next iteration. The coefficient λ is an under-relaxation factor that can be applied to provide stability to the computation if necessary,

$$x_s = x_s + \lambda dx_s. \quad (7)$$

Once x_s is updated, the process is repeated through successive iterations until the error reaches a minimum. Since the minimum error may differ from one time instant to the next and its value is not known *a priori*, we define the following residual to determine whether the solution has converged:

$$r \equiv |E_{n+1} - E_n|, \quad (8)$$

where the error E is defined by

$$E \equiv \sum_{i=1}^4 e_i^2. \quad (9)$$

Convergence was based on a set limit of $r \leq 10^{-10}$.

B. Method II

The first method is a simple and computationally efficient approach to shock tracking that may potentially be useful in other shock-containing flowfields. It does have some obvious disadvantages, however, when applied to the specific case of shock waves in nozzle flow. One disadvantage is that the hyperbolic tangent function does not account for pressure gradients in the flowfield upstream or downstream of the shock wave. These gradients can be significant in the case of nozzle flow, particularly in the expansion region upstream of the shock. Using a model distribution that does not account for these gradients leads to inherent error in the tracking process. Also, stability issues with the least-squares scheme

used in the first method limit the number of parameters that can effectively be varied in the minimization process. Fluctuation in the magnitude and thickness of the pressure jump across the shock foot are thus accounted for using approximations.

The second method we present addresses the concerns stated above by implementing a more adaptive model distribution as well as a more sophisticated minimization scheme capable of varying additional parameters. The pressure distribution caused by the shock footprint is still approximated using a hyperbolic tangent function, although an exponential function has been included to shape the curve before and after the pressure jump. The modified pressure distribution shown in Eq. (10) better reflects the expansion, jump, and recovery sequence that is typical of shock-containing nozzle flow,

$$P(x, Q_k) = \bar{p}_j + \frac{\Delta p}{2} \{1 - \exp[-c_1(x - x_o + c_2)]\} \times \tanh\left[\frac{2}{\delta_o}(x - x_o)\right], \quad (10)$$

where Q_k is the parameter vector

$$Q_k = [x_o \ \bar{p}_j \ \Delta p \ \delta_o \ c_1 \ c_2]. \quad (11)$$

The first four parameters of the above vector approximately represent the shock location, the mean pressure of the jump, the magnitude of the jump, and the thickness of the jump, respectively. Differences between these values and the actual values, as defined in the first method, are a consequence of the exponential term in the distribution. The last two parameters are constants of the exponential that can be appropriately tuned to account for the pressure gradients upstream and downstream of the pressure jump. Unlike the first method, all six parameters of the distribution are varied to fit the model curve to the measured distribution. The actual shock location x_s , as defined by the location of the inflection point of the distribution, is easily recovered at minimal additional computational cost.

Similar to before, we seek to minimize the error between the model distribution and the actual distribution measured from experiment. To do this we define the following cost function which measures the absolute difference between the modeled and experimental distributions:

$$E \equiv \sum_{i=1}^5 [p_i - P(x_i, Q_k)]^2. \quad (12)$$

A “ghost” point is added to the instantaneous pressure distribution to help stabilize the curve upstream of the shock. The pressure at this point is based on mean wall pressure data from a previous investigation.⁴

For each time sample a multivariable, constrained minimization of the cost function was performed using the robust MATLAB function *fmincon* from the Optimization Toolbox.TM This function uses an active-set algorithm that is described in detail in Refs. 21 and 22. Since *fmincon* performs a constrained minimization, the upper and lower bound of each parameter were set to physically reasonable values.

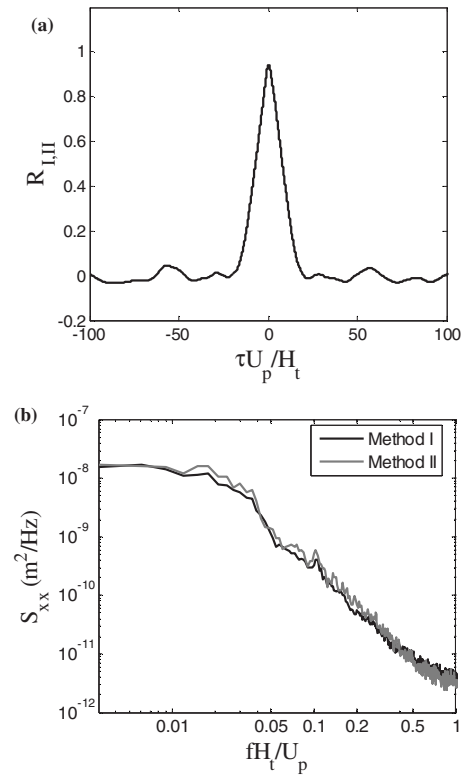


FIG. 11. Comparison of the shock tracking methods: (a) cross correlation of signals from methods I and II; (b) autospectra of shock motion resulting from the two methods.

C. Comparison and validation

A comparison of the two shock tracking methods, applied to case 3 (Table I), is shown in Fig. 11. Figure 11(a) shows the cross correlation of the shock position signals obtained using the two different methods. The two signals are nearly perfectly correlated. Figure 11(b) shows the autospectra of the two signals. The autospectra essentially overlap, meaning the signals also have the same frequency content. This excellent agreement between the results of the two tracking methods provides confidence on their accuracy. Given that the methods differ significantly, there is a far greater likelihood that they both result in the same accurate position signal than the likelihood that they produce the same error. While the first method is computationally faster, the model distribution used in the second method is specific to nozzle flow and therefore has been used in the remainder of this study.

Figure 12 shows a visual depiction of the second shock tracking method applied to case 3. The last frame at the bottom of the figure plots the shock position time trace. The first four frames of the figure show instantaneous pressure distributions corresponding to times $t=t_1, t_2, t_3$, and t_4 noted by vertical dashed lines on the shock position trace. The instantaneous experimental pressure distribution measured by the wall transducer array $p(x_i)$ is plotted along with the fitted function $P(x, Q_k)$. The thin vertical line in each of the first four frames indicates the location of the shock x_s , as defined by the inflection point of $P(x, Q_k)$.

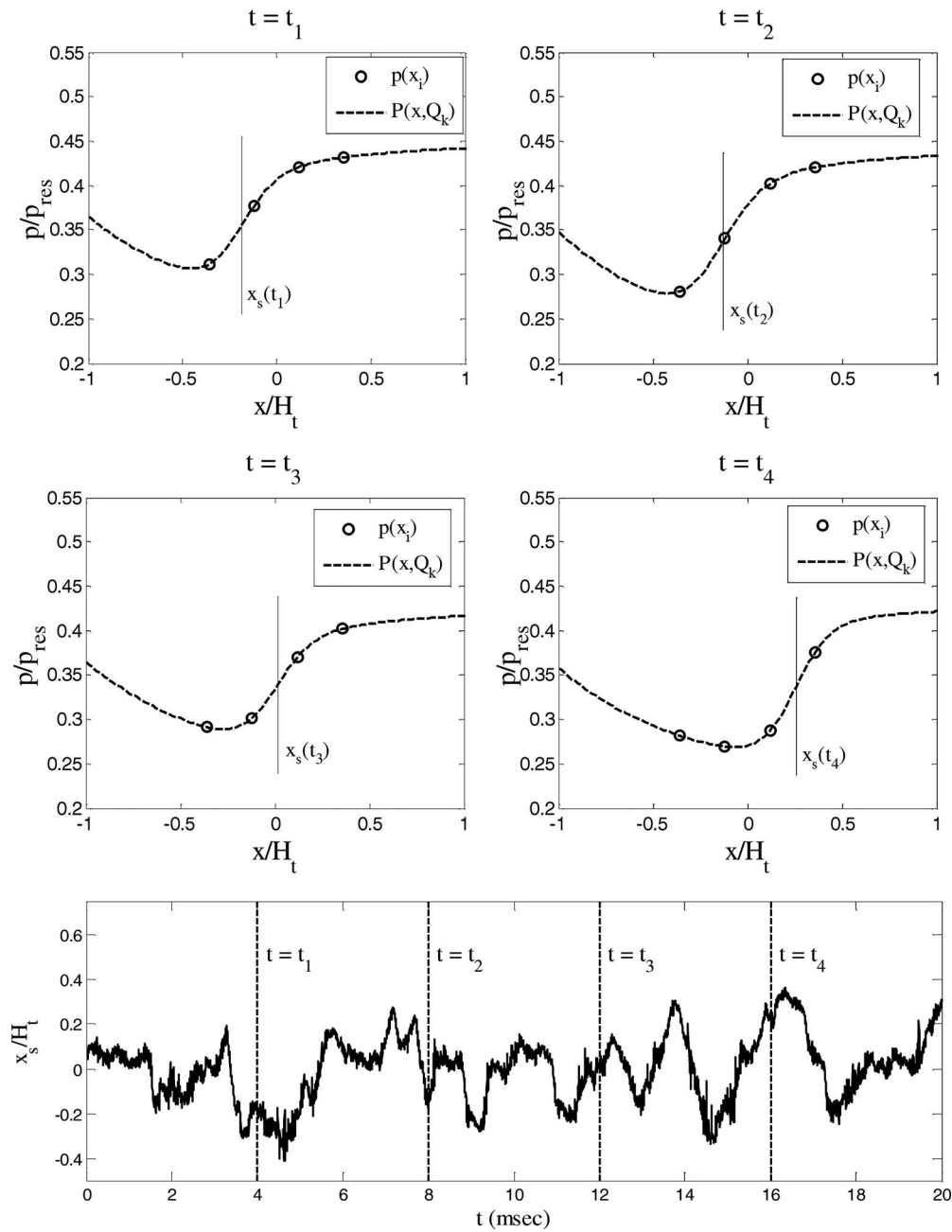


FIG. 12. Illustrative pressure snapshots and time trace from shock tracking method II applied to case 3.

IV. RESULTS

A. Statistics of shock motion

The shock position trace and probability density function for case 1 are shown in Figs. 13(a) and 13(b), respectively. For this relatively weak shock, separation is moderately asymmetric. The shock position signal is characterized by small-scale oscillations about the preferred, or equilibrium shock position, with occasional large-scale perturbations primarily in the upstream direction. This behavior is reflected in the asymmetry of the probability density function, where the peak value occurs at a normalized position that is greater than zero. This means that the equilibrium shock location is slightly downstream of the mean shock location. The notice-

able skewness in the plot of Fig. 13(a) ($Sk/\sigma^3 \approx -0.8$) is the result of the occasional large-scale fluctuation toward the upstream direction.

As the nozzle area ratio and NPR are increased, the shock becomes stronger. The resulting effect on the shock motion can be seen in the position trace of Fig. 14 for case 3. There is an obvious increase in both the range of the shock motion and the frequency of large-scale motions. The result is an increase in the root mean square of the fluctuation and a reduction in the magnitude of the skewness of the signal ($Sk/\sigma^3 \approx -0.3$). Thus, the shock becomes less stable with increasing shock strength. This trend has been noticed in various other shock-containing flowfields.¹⁴ We quantify

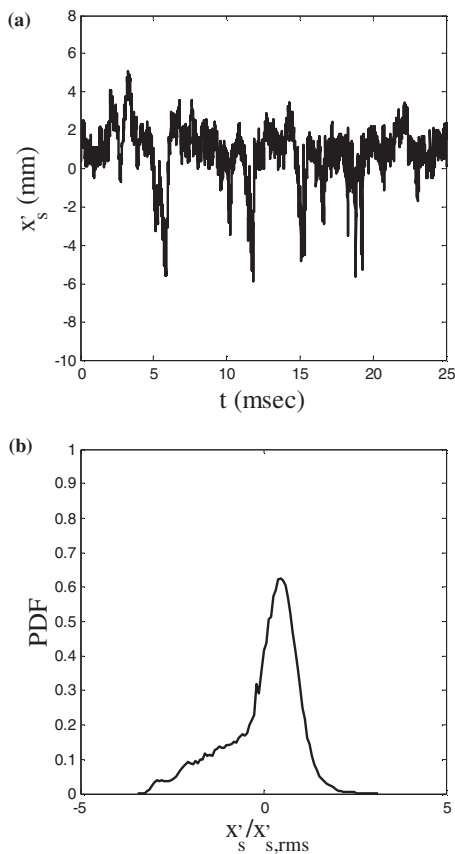


FIG. 13. (a) Shock-position fluctuation trace and (b) corresponding probability density function for case 1.

these trends by plotting the rms and peak-to-peak amplitudes of the shock location versus shock strength in Figs. 15 and 16, respectively. For the stronger shocks, the peak-to-peak amplitude of shock motion is of the same order as the nozzle throat height.

The spectra of the shock position fluctuation for cases 1–4 are plotted in Fig. 17. With increasing shock strength, the amplitude of shock motion increases for nondimensional frequency $fH_t/U_p < 0.05$. For higher frequency the amplitude is practically unchanged. The values of nondimensional frequency where the shock motion increases are consistent with the shock excitation Strouhal numbers on the order of

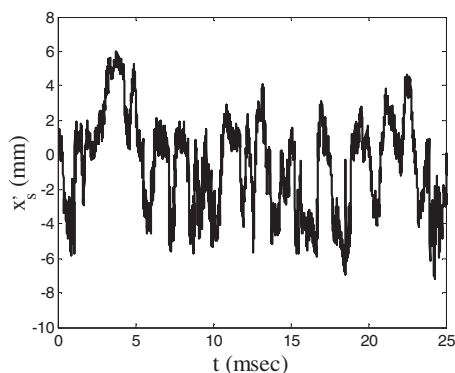


FIG. 14. Shock position fluctuation for case 3 showing increased shock instability.

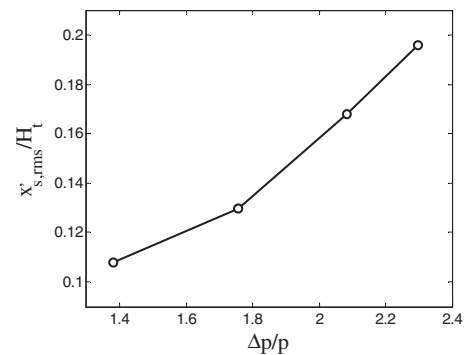


FIG. 15. Root mean square of the shock position fluctuation vs shock strength.

10^{-2} in the review article by Dussauge and Piponniau.¹⁵ It is important to note that the spectra are broadband with no pronounced peaks or bumps such as the ones noticed in the experiments by Bourgoing and Reijasse.¹⁶ This implies that for the conditions of this experiment, the unsteadiness is not governed by any resonant interactions, but rather by random fluctuations.

B. Correlations between shock motion and plume total pressure

In this section we study correlations between the shock motion and the fluctuating total pressure as measured by the dynamic Pitot probe at various points in the separated flow. The coordinate system and positions of the Pitot probe are shown in Fig. 18. We first consider the nature of the fluctuations downstream of the shock. Figure 19 shows the spectrum of total pressure fluctuations for case 3 at the exit of the nozzle near the large separation shear layer ($X/H_t=0.0$, $Y/H_t=0.32$). The shape of the spectrum is similar to that of the shock position spectrum shown in Fig. 15(a), where the highest spectral intensity occurs at low frequency. The primary difference in the shape of the spectra is the slight increase in intensity in the mid to high frequency range of the total pressure spectrum, which may be associated with the presence of broadband turbulent fluctuations in the shear layer.

For the following correlations, the Pitot probe was at a fixed position one exit height upstream of the nozzle exit, measuring in the large separation shear layer downstream of

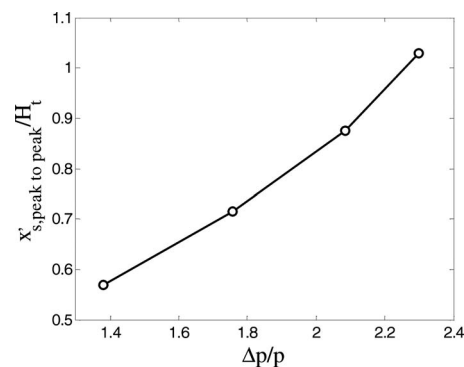


FIG. 16. Peak-to-peak shock displacement vs shock strength.

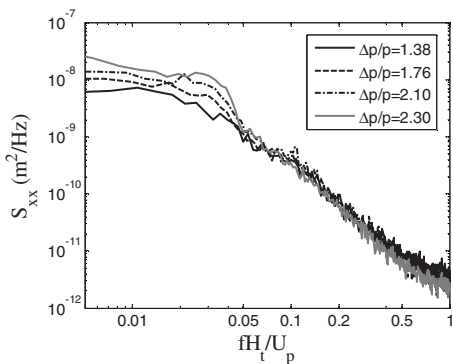


FIG. 17. Typical autospectra of the shock position fluctuation for cases 1–4.

the shock ($X/H_t = -1$, $Y/H_t = 0.32$). First consider case 1, where the shock motion is relatively weak. Figure 20(a) shows the correlation of the shock motion with the total pressure fluctuation. It is practically zero, indicating no significant interaction. In case 3, where the shock motion is strong with frequent large amplitude motions, the correlation becomes substantial, as shown in Fig. 20(b). The frequency content of this cross correlation can be found by plotting the coherence between the shock motion and the total pressure fluctuations, presented in Fig. 21. The coherence is significant (>0.1) for nondimensional frequency less than 0.05. This is the same frequency range of enhanced shock motion noted in Fig. 17. We thus infer that the shock motion-total pressure correlation is driven by the large-amplitude, low-frequency motion of the shock that becomes more prevalent with increasing shock strength.

To further test this hypothesis, we produced spatial maps of shock motion-total pressure correlation with increasing shock strength. The Pitot probe was traversed through the internal and external flows according to the grid of Fig. 18. We define the correlation “peak” as the maximum value of the correlation, if it is positive, or its minimum value, if it is negative. Figures 22(a)–22(d) show contour plots of the correlation peaks for cases 1–4, respectively. The contour plots include the outline of the nozzle (solid lines) and the approximate position of the shock (dashed lines). As the shock strength increases the correlation between shock motion and total pressure fluctuation in the separation shear layer becomes stronger and extends over a larger spatial range. For case 4, the peak correlation is as high as 0.4 at two throat

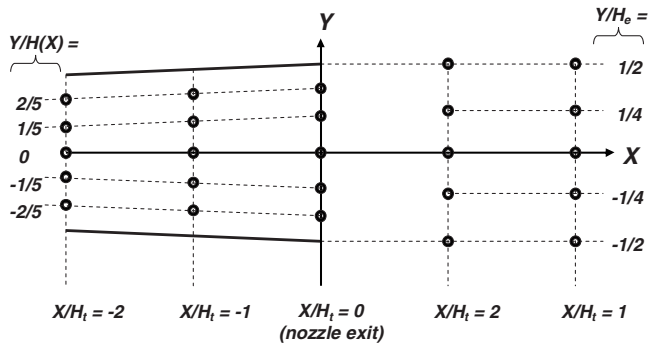


FIG. 18. Coordinate system and positions of Pitot probe.

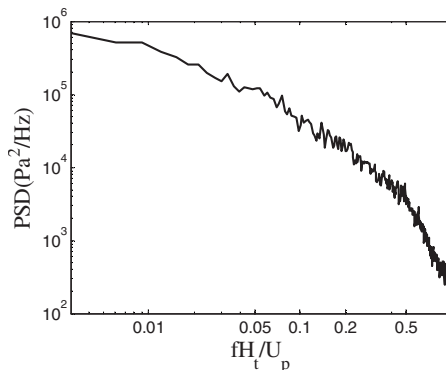


FIG. 19. Autospectrum of total-pressure fluctuation for case 3 at probe position $X/H_t = 0.0$ and $Y/H_t = 0.32$.

heights downstream of the nozzle exit. Comparison of the correlation plots with the distribution of mean total pressure inside the nozzle indicates that the correlation peaks near the dividing streamline of the shear layer. An additional trend in Figs. 22(a)–22(d) is the negative correlation along the nozzle centerline, which grows with increasing shock strength. In general, this negative correlation is smaller in magnitude than the positive correlation measured in the shear layer. The negative correlation is the result of the shock motion on the “potential” core of the separation jet: when the shock moves downstream (positive x -direction, higher A_s/A_t) it becomes stronger (higher total pressure loss), resulting in a negative perturbation of the total pressure downstream. The opposite occurs when the shock is perturbed upstream. In other words,

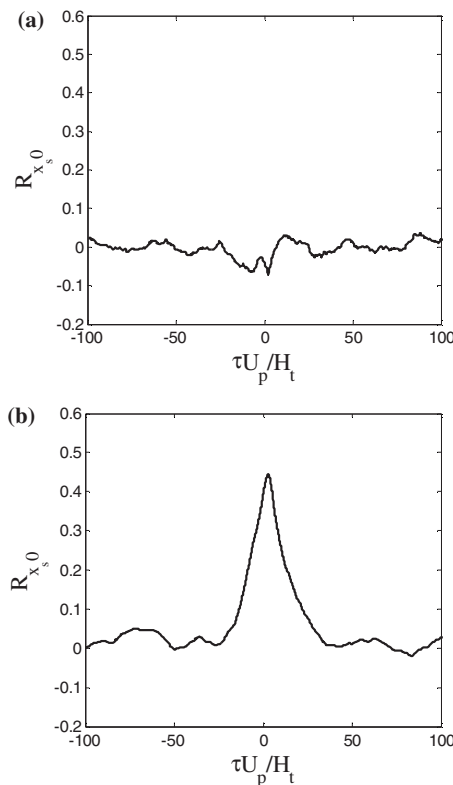


FIG. 20. Cross correlation of shock position and total-pressure fluctuation measured in the large separation shear layer for (a) case 1; (b) case 3.

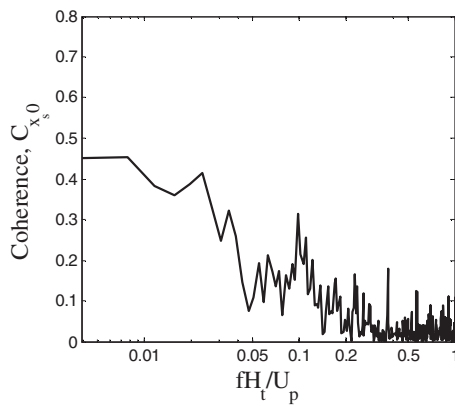


FIG. 21. Coherence of shock position and total-pressure fluctuation measured in the large separation shear layer for case 3.

the negative correlation is a predictable phenomenon one can explain using one-dimensional shock theory. On the other hand, the positive correlation in the shear layer is a nontrivial consequence of the shock motion inducing large-scale turbulent eddies. Since the shock defines the origin of the shear layer, one could think of the shock motion as a means of forcing (analogous perhaps to moving the splitter plate tip in a shear layer experiment²³) that can increase the instability and growth rate of the shear layer. Our experiment suggests that the separation shear layer is highly receptive to low-frequency, large-amplitude oscillations that become more prevalent as the shock strength increases.

C. Effect of the alternating wave pattern

We turn now to the separate experiment that involved the interaction of a sonic shear layer with a pattern of stationary waves emanating from a wavy wall. As described previously, the experiment was designed to simulate the isolated effect of the alternating compression and expansion waves, generated downstream of the main shock, on the stability of the separation shear layer. Flow visualization was used to qualitatively assess the impact of the periodic wave pattern on the stability of the shear layer. Figures 23(a) and 23(b) show schlieren images of the test section of the shear layer facility with a flat upper wall and a wavy upper wall, respectively. We observe waves in both cases, but their nature is different. In the baseline (flat-wall) case the waves are weak and result from the interaction between the pressure field of the turbulent structures and the upper boundary. As such, they are not periodic but rather randomly distributed in the test section. In the case of the wavy wall, the wall perturbation produces strong periodic waves comprising an alternating pattern of compressions and expansions. It should also be noted that the waves in the baseline case are convected downstream with the speed of the shear layer structures, whereas the waves in the wavy wall case are stationary in the laboratory frame and therefore stronger. The wall disturbances do not appear to significantly alter the stability of the flowfield. There is no noticeable difference in the growth rates or turbulent structures of the shear layers in the two cases.

To obtain quantitative measures of instability, the dynamic Pitot probe was used to measure the time-resolved

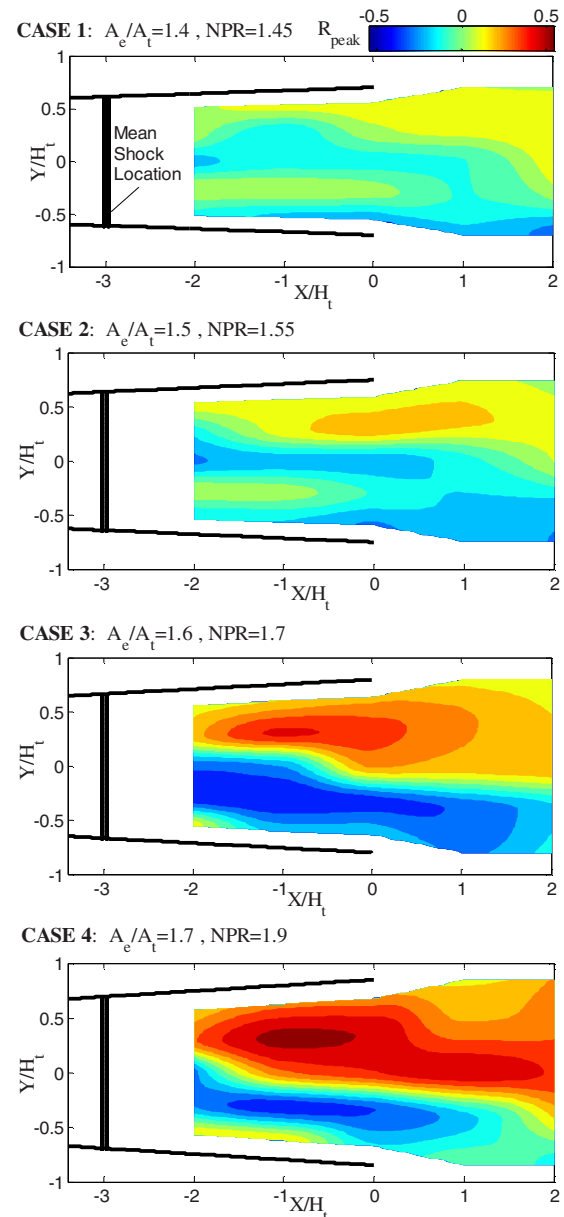


FIG. 22. (Color online) Contour plots of peak $x_s-p'_0$ correlation for the cases of this study in order of increasing shock strength.

total pressure distribution across the test section at a downstream distance of $X=4.0H_u$ from the tip of the splitter plate. Figure 24(a) shows the mean total pressure profile of the baseline and wavy wall cases. The baseline case shows the typical hyperbolic tangent distribution, whereas the profile of the wavy wall case shows noticeable differences. First, there is an obvious reduction in the peak, mean total pressure in the wavy wall case compared with the baseline case. This is a result of total pressure losses in the upper stream caused by the succession of shocks generated by the sinusoidal wall. The drop in total pressure is accompanied by an increase in the static pressure of the upper stream causing the dividing streamline in the wavy wall case to bend toward the lower wall with downstream distance. This effect is evident from the displacement in the location of the inflection point between two profiles. There is also a slight drop in mean pres-

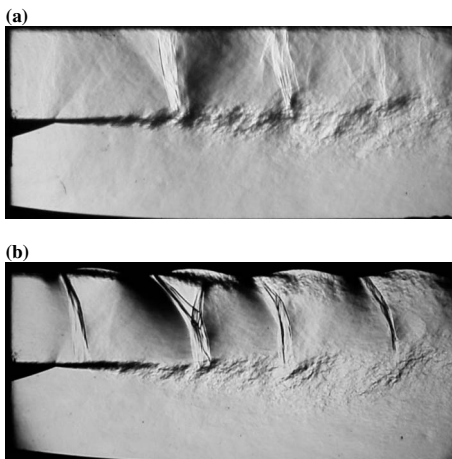


FIG. 23. Schlieren images of sonic shear layer with (a) flat and (b) wavy upper wall.

sure in the wavy wall case very close to the wall, likely resulting from the effects of flow separation seen clearly in the schlieren images. This drop in pressure is not present in the baseline profile where the flow remains attached to the upper wall.

The corresponding distributions of root mean square of the total pressure fluctuation are plotted in Fig. 24(b). There are no increases in rms levels between the baseline and wave wall cases that would imply increased instability due to the imposed wave pattern. The primary differences between the two plots are the shift between the peak rms locations (due to

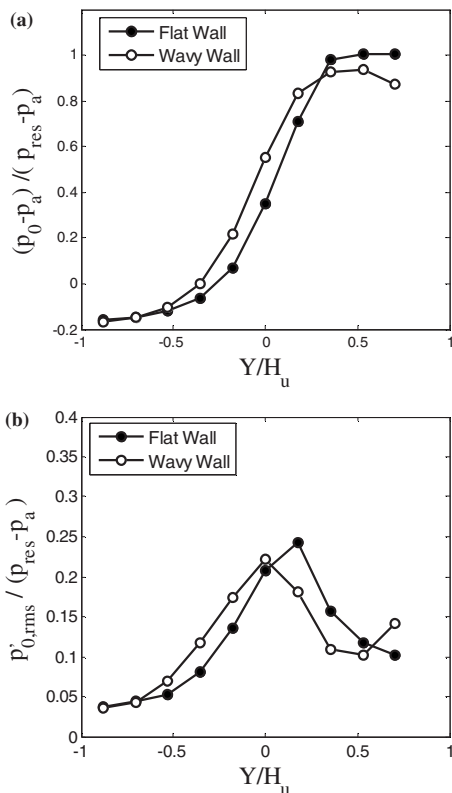


FIG. 24. Transverse distribution of (a) mean total pressure and (b) rms pressure at an axial distance of $X/H_u=4.0$.

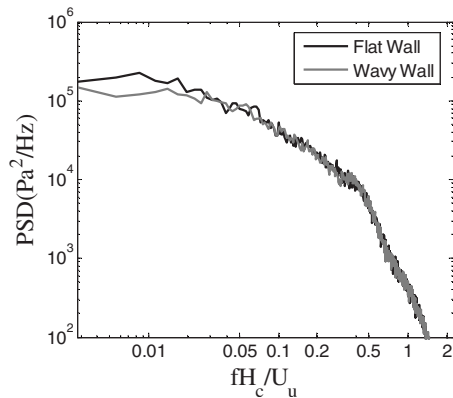


FIG. 25. Autospectrum of total-pressure fluctuation at the maximum rms location in the shear layer at an axial position of $X/H_u=4.0$.

the bending of the dividing streamline) and a slight increase in rms level near the wavy wall due to the presence of separation. The total pressure spectra at the peak rms location are shown in Fig. 25 for both cases. The spectrum for the wavy wall case nearly perfectly overlaps with the spectrum for the baseline case. Therefore, not only is the average intensity of the pressure fluctuation the same for both cases, but the frequency content of each signal is identical as well.

The experiments indicate a complete lack of receptivity of the sonic shear layer to the strong disturbances generated by the wavy wall. Extrapolating these results to shock-containing nozzle flow, it appears highly unlikely that the wave pattern downstream of the separation shock, by itself, is responsible for generating the instability observed in Figs. 1 and 2.

V. CONCLUSION

We have conducted a two-part investigation in order to identify the primary mechanisms that contribute to unsteadiness in the jet plume emerging from a shock-containing convergent-divergent nozzle. The first part considered shock-containing nozzle flow directly and involved time-resolved, simultaneous measurements of the shock motion and the total pressure in the flow downstream of the shock. Four combinations of NPR and nozzle area ratio were tested resulting in progressively stronger shock waves. The second part considered the isolated impact of the series of compressions and expansions that follow the main shock on the stability of the separation shear layer. This was conducted in a separate facility wherein a sonic shear layer, simulating the nozzle separation shear layer, was disturbed with compression and expansion waves emanating from a wavy wall. The key findings of these experiments are as follows.

The shock motion is broadband and its low-frequency content increases with shock strength. The total pressure fluctuations in the separated flow are broadband as well. A strong correlation between the shock motion and total pressure fluctuation in the large separation shear layer is observed for shock strength $\Delta p/p \geq 2.0$. The coherence of the signals indicates that the correlation is associated with low-frequency, large-scale motion of the shock. The magnitude

and downstream spatial extent of the correlation between the shock motion and total pressure fluctuation increase with increasing shock strength. The correlation peaks near the dividing streamline of the large shear layer, suggesting that the shock motion acts as a forcing function driving the instability.

No significant correlations between shock motion and plume total pressure were measured for $\Delta p/p \leq 1.8$. This suggests that there are likely two factors that contribute to a strong correlation and hence increased persistence of the instability into the downstream flow. First, as shock strength is increased the amplitude of the shock motion becomes larger, forcing larger-amplitude instability waves. Second, as shock strength is increased the shock/separation structure becomes asymmetric allowing more space for instability waves to grow in the large separation shear layer.

The experiments in the shear layer facility revealed that when isolated from the unsteady shock motion, the alternating series of expansion and compression waves present downstream of the main separation shock likely has no significant impact on the stability of the downstream shear flow. This suggests that the increased amplitude of shock motion is the primary mechanism contributing to the increased unsteadiness, and thus mixing enhancement, observed in jets exhausting from shock-containing convergent-divergent nozzles.

ACKNOWLEDGMENTS

We are grateful for the support by the National University of Singapore, Temasek Laboratories (Contract No. TL/AE/2004/0001) monitored by Dr. Her Mann Tsai.

¹J. Ostlund and B. Muhammad-Klingmann, "Supersonic flow separation with application to rocket engine nozzles," *Appl. Mech. Rev.* **58**, 143 (2005).

²D. Papamoschou, "Mixing enhancement using axial flow," AIAA Paper No. 2000-0093, 2000.

³E. Murakami and D. Papamoschou, "Experiments on mixing enhancement in dual-stream jets," AIAA Paper No. 2001-0668, 2001.

⁴M. Debiase, S. S. Dhanabalan, H. M. Tsai, and D. Papamoschou, "Mixing

enhancement of high-bypass turbofan exhausts via contouring of fan nozzle," AIAA Paper No. 2007-4497, 2007.

⁵K. B. M. Q. Zaman and D. Papamoschou, "Study of mixing enhancement observed with a co-annular nozzle configuration," AIAA Paper No. 2000-0094, 2000.

⁶D. Papamoschou, A. Zill, and A. Johnson, "Supersonic flow separation in planar nozzles," *Shock Waves* **19**, 171 (2009).

⁷R. G. Wilmoth and L. D. Leavitt, "Navier-Stokes prediction in multi-function nozzle flows," *SAE Trans.* **96**, 6.865 (1987).

⁸A. Hamed and C. Vogiatzis, "Overexpanded two-dimensional convergent-divergent nozzle flow simulations, assessment of turbulence models," *J. Propul. Power* **13**, 444 (1997).

⁹A. Hamed and C. Vogiatzis, "Overexpanded two-dimensional convergent-divergent nozzle flow performance, effects of three-dimensional flow interactions," *J. Propul. Power* **14**, 234 (1998).

¹⁰H. Li and G. Ben-Dor, "Mach reflection wave configuration in two-dimensional supersonic jets of overexpanded nozzles," *AIAA J.* **36**, 448 (1998).

¹¹G. L. Romine, "Nozzle flow separation," *AIAA J.* **36**, 1618 (1998).

¹²Q. Xiao, H. M. Tsai, and D. Papamoschou, "Numerical investigation of supersonic nozzle flow separation," *AIAA J.* **45**, 532 (2007).

¹³D. Papamoschou and A. Johnson, "Unsteady phenomena in supersonic nozzle flow separation," AIAA Paper No. 2006-3360, 2006.

¹⁴J. P. Dussauge, P. Dupont, and J. F. Debieve, "Unsteadiness in shock wave boundary layer interaction with separation," *Aerosp. Sci. Technol.* **10**, 85 (2006).

¹⁵J. P. Dussauge and S. Piponniau, "Shock/boundary-layer interactions: Possible sources of unsteadiness," *J. Fluids Struct.* **24**, 1166 (2008).

¹⁶A. Bourgoing and Ph. Reijasse, "Experimental analysis of unsteady separated flows in a supersonic planar nozzle," *Shock Waves* **14**, 251 (2005).

¹⁷K. B. M. Q. Zaman, M. D. Dahl, T. J. Bencic, and C. Y. Loh, "Investigation of a 'transonic resonance' with convergent-divergent nozzles," *J. Fluid Mech.* **463**, 313 (2002).

¹⁸Q. Xiao, H. M. Tsai, and D. Papamoschou, "Numerical study of jet plume instability from an overexpanded nozzle," AIAA Paper No. 2007-1319, 2007.

¹⁹C. K. W. Tam and F. Q. Hu, "Resonant instability of ducted free supersonic mixing layers induced by periodic Mach waves," *J. Fluid Mech.* **229**, 65 (1991).

²⁰M. J. Doty and D. K. McLaughlin, "Experiments on Mach-wave interactions in a compressible shear layer," *AIAA J.* **38**, 1871 (2000).

²¹P. E. Gill, W. Murray, and M. H. Wright, *Practical Optimization* (Academic, New York, 1981).

²²M. J. D. Powell, "A fast algorithm for nonlinearly constrained optimization calculations," *Numerical Analysis*, Lecture Notes in Mathematics, edited by G. A. Watson (Springer, New York, 1978).

²³D. Oster and I. Wygnanski, "The forced mixing layer between parallel streams," *J. Fluid Mech.* **123**, 91 (1982).